Journal of Metals, Materials and Minerals, 37(1), e2614, 2027

Tailoring mechanical response of AA8006 aluminum alloy through severe cold rolling: A process–structure–property study

Narin JANTAPING[1,2], and Man TUIPRAE[1,2,*]

[1] *Research, Innovation Unit of Rail System and Testing (RU-RailS), Center of Excellence in Professional Skills and Technology, Faculty of Engineering, Rajamangala University of Technology Lanna, Chiang Mai, Thailand, 128 Huay Kaew Road, Muang, Chiang Mai, Thailand, 50300*
[2] *Department of Industrial Engineering, Faculty of Engineering, Rajamangala University of Technology Lanna, Chiang Mai, Thailand, 128 Huay Kaew Road, Muang, Chiang Mai, Thailand, 50300*

***Corresponding author e-mail**: tman@rmutl.ac.th

Received date:
25 December 2025
Revised date:
29 March 2026
Accepted date:
24 October 2026

Keywords:
Al–Fe–Si-based alloys;
Cold rolling;
Work hardening;
Crystallographic texture;
Electron backscatter diffraction

Abstract

This study investigates the process–structure–property relationships of AA8006 aluminum alloy processed by twin-roll casting followed by cold rolling with thickness reductions ranging from 0% to 97%. Microstructural characterization reveals progressive grain elongation and fragmentation of Al–Fe–Mn–Si intermetallic particles with increasing deformation. These microstructural changes are accompanied by a continuous increase in tensile strength from 156 MPa to 280 MPa and a significant increase in hardness, primarily attributed to work hardening and particle–dislocation interactions. Crystallographic characterization using X-ray diffraction (XRD) and electron backscatter diffraction (EBSD) demonstrates substantial texture evolution and grain subdivision during cold rolling, indicating the development of deformation-induced microstructures. The combined microstructural, mechanical, and crystallographic analyses provide a comprehensive understanding of the strengthening mechanisms and deformation behavior of severely cold-rolled AA8006 alloy, offering useful insights for optimizing thermomechanical processing routes in non-heat-treatable aluminum alloys.

1. Introduction

Aluminum and its alloys are cornerstone materials for modern engineering, prized for their favorable strength-to-weight ratio, corrosion resistance, and formability [1]. A substantial portion of industrial aluminum is processed into flat-rolled products—sheets, plates, and foils—via rolling operations, where final properties are intricately linked to the induced microstructure and crystallographic texture [2]. Among the various aluminum grades, the AA8006 series (Al–Fe–Mn–Si system) is a non-heat-treatable alloy specifically designed for applications requiring a balance of moderate strength, good thermal conductivity, and formability, such as heat exchanger fins and automotive components [3,4].

Recent studies have demonstrated that cold rolling of aluminum alloys promotes pronounced β-fiber texture development and significant grain refinement, both of which strongly influence the resulting mechanical properties. For example, Zulai Li *et al.* [5] investigated the microstructure, texture evolution mechanisms, and mechanical properties of cryogenically rolled and micro-thermally aged AA6061 alloys. Similarly, in Al–Fe–Si-based alloys, comparable texture transitions and particle evolution during thermomechanical processing were reported by Ranjeet Kumar [6]. The industrial manufacturing of AA8006 sheet frequently utilizes the twin-roll casting (TRC) process, an energy-efficient method that directly produces a thin strip, which is subsequently cold-rolled and annealed to final gauge [7]. Cold rolling is not merely a dimensional reduction step; it is a severe plastic deformation process that fundamentally alters the material's state. It introduces a high density of dislocations (work hardening), refines and redistributes second-phase particles, and, most critically, reorients the crystalline lattice of the individual grains, developing a non-random crystallographic texture [8,9]. Crystallographic texture influences deformation behavior and mechanical properties [10,11]. In the present study, tensile properties were evaluated only along the rolling direction (RD), and the analysis therefore focuses on tailoring the mechanical response along RD.

While the principles of texture evolution in face-centered cubic (FCC) metals like aluminum during cold rolling are well-established, leading to the characteristic β-fiber running from the Brass ({110}<112>) through the S ({123}<634>) to the Copper ({112}<111>) orientation [12,13], their specific manifestation in commercial AA8006 alloy remains insufficiently documented. A detailed, quantitative investigation correlating the degree of cold-rolling reduction with the concurrent evolution of microstructure, macrotexture, microtexture, and mechanical properties in this industrially relevant alloy is lacking [14–16].

Therefore, this work presents a comprehensive study on AA8006, subjecting twin-roll cast material to a wide range of cold-rolling reductions (0% to 97%). The objective is to quantitatively establish the process-structure-property relationships by integrating mechanical testing (tensile, hardness), microstructural analysis (optical microscopy

and scanning electron microscopy (SEM)), macrotexture characterization (X-ray diffraction (XRD) pole figures), and local microtexture analysis (electron backscatter diffraction (EBSD)). This holistic approach aims to provide a foundational framework for understanding and tailoring the mechanical properties along RD of AA8006 through controlled thermomechanical processing.

2. Experimental procedure

2.1 Material and processing

The AA8006 aluminum alloy used in this investigation was supplied by the Department of Metallurgical Engineering, Chulalongkorn University, Thailand. Its chemical composition, determined by optical emission spectrometry, is presented in Table 1. The material was initially produced via a continuous TRC process with a casting temperature of 686°C and a roll speed of 10.4 m·min^{-1} (34 ft min^{-1}), yielding an as-cast strip with a nominal thickness of 6.5 mm. Subsequent cold rolling was performed on a laboratory two-roll mill at room temperature. The 6.5 mm thick as-cast strip was subjected to a series of passes to achieve varying levels of thickness reduction. The final thickness reductions were 0% (as-cast reference), 61%, 71%, 83%, and 97%. The percentage thickness reduction, R, was calculated using Equation (1):

$$R = \frac{t_0 - t_f}{t_0} \times 100\% \quad (1)$$

where R is the percentage thickness reduction, t_0 is the initial strip thickness (6.5 mm), and t_f is the final thickness after cold rolling.

2.2 Mechanical testing

Uniaxial tensile tests were conducted at room temperature using an Instron 55R4502 universal testing machine. Tensile testing was performed in accordance with ASTM E8/E8M. Flat tensile specimens, with their gauge length aligned parallel to RD, were tested at a constant crosshead speed of 10 mm·min^{-1}. Yield strength (YS, determined using the 0.2% offset method) and ultimate tensile strength (UTS) were determined from the resulting stress-strain curves. Vickers microhardness (HV) measurements were performed on the RD–transverse direction (TD) plane (i.e., the plane whose normal is parallel to the normal direction (ND)) using an Anton-Paar MHT-10 microhardness tester. Vickers hardness measurements followed ASTM E92. A load of 200 gf was applied with a dwell time of 15 s. At least ten indentations were made for each condition to ensure statistical reliability, and the average value is reported.

2.3 Microstructural and crystallographic characterization

For metallographic examination, samples were sectioned, mounted, mechanically ground, polished to a 1 μm finish. Keller's reagent was used for metallographic etching. The reagent composition consisted of 190 mL distilled water, 5 mL HNO_3, 3 mL HCl, and 2 mL HF, and the specimens were etched by immersion for 10 s to 20 s at room temperature [17]. Initial microstructural observation was carried out using an Olympus BHM optical microscope.

Table 1. Chemical composition of the aluminum AA8006 (wt%).

Chemical composition [wt%]						
Si	**Fe**	**Cu**	**Mn**	**Mg**	**Ti**	**Al**
0.131	1.340	0.037	0.378	<0.001	0.033	Bal.

Macrotexture (bulk texture) analysis was performed using XRD on a Rigaku TTRAX III diffractometer equipped with a Cu Kα X-ray source (λ = 1.5406 Å) operated at 50 kV and 300 mA. Incomplete pole figures for the {111}, {200}, {220}, and {311} crystallographic planes were measured in reflection geometry on the sample surface, with its normal parallel to ND. Measurements covered the orientation hemisphere with the tilt angle (α) ranging from 0° to 90° and the azimuthal angle (β) from 0° to 360°, using a step interval of 5°. The raw intensity data were processed, and three-dimensional pole figures were constructed using Rigaku's 3D Explore software (v2.3).

The texture coefficient (TC), denoted $TC_{(hkl)}$, was calculated to quantify the orientation preference using Equation (2) [18]:

$$TC_{(hkl)} = \frac{I_{(hkl)}/I_{r,(hkl)}}{\frac{1}{n}\sum(I_{(hkl)}/I_{r,(hkl)})} \quad (2)$$

where $I_{(hkl)}$ is the measured intensity of the (hkl) reflection, $I_{r,(hkl)}$ is the standard intensity from a powder diffraction file (JCPDS #04-0787 for Al), and n is the number of reflections considered. A TC value of 1 indicates a random orientation.

For local microtexture and orientation analysis, EBSD was performed using a Hitachi S-3400N scanning electron microscope equipped with an EDAX Hikari EBSD camera. Before EBSD analysis, specimens were polished with a 50% colloidal silica (0.05 μm) slurry using a vibration polishing machine operated at 50 Hz [19]. Measurements were conducted at an accelerating voltage of 20 kV, a tilt angle of 70°, and with a step size of 0.07 μm. The acquired EBSD data were analyzed using OIM Analysis™ software (TSL, v6.0) to generate inverse pole figure (IPF) maps and determine grain boundary misorientation distributions. A minimum misorientation angle of 5° was used to define grain boundaries.

3. Results and discussion

3.1 Microstructural evolution

Figure 1 presents optical micrographs of AA8006 in the as-cast (0% reduction) and cold-rolled (61% and 97% reduction) conditions, viewed on the RD-ND plane. The as-cast microstructure (Figure 1(a)) exhibits a typical cast structure with coarse, elongated grains along the casting/rolling direction. Dark-contrast second-phase particles, predominantly Al-Fe-Mn-Si intermetallics characteristic of the 8xxx series alloys, are aligned in stringers parallel to the RD which is identified that based on literature-supported interpretation by P. Moldovan, *et al.* [20,21]. With cold rolling, a profound microstructural refinement occurs. At 61% reduction (Figure 1(b)), the original grains are significantly elongated into a lamellar structure. The second-phase particles begin to fragment and align more densely within the deformation bands. After 97% reduction (Figure 1(c)), the microstructure is highly refined, appearing as a dense, fibrous array of

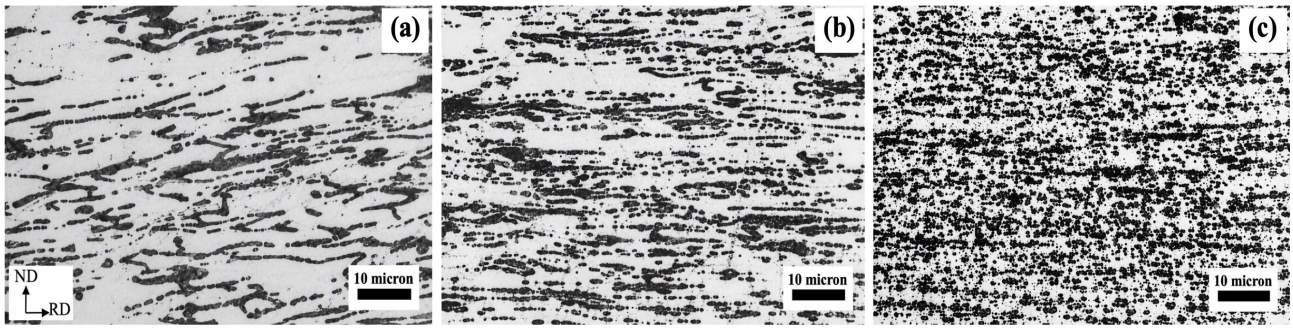


Figure 1. Optical micrographs of AA8006 at different cold-rolling reductions: (a) 0%, (b) 61%, and (c) 97%.

deformation bands. The second-phase particles are further fragmented and more uniformly distributed. This evolution is consistent with the well-known mechanisms of particle shearing and fragmentation during severe plastic deformation, where high strain energy overcomes the strength of brittle intermetallics, creating finer, more potent obstacles for dislocation motion [20].

3.2 Mechanical properties

The mechanical response of AA8006 is strongly governed by the degree of cold work, as shown in Figure 2. Both YS and UTS increase monotonically with rolling reduction (Figure 2(b)). The as-cast material exhibits a UTS of approximately 156 MPa, which rises to 280 MPa after 97% reduction—an increase of nearly 80%. A similar trend is observed for Vickers microhardness (Figure 3), which escalates from 54 HV to 87 HV over the same reduction range. This pronounced strengthening is a classical manifestation of work (or strain) hardening. Cold rolling introduces a high density of dislocations, and their mutual interactions (tangling, pile-ups) significantly increase the stress required for further plastic deformation [22]. Furthermore, the refined and dispersed second-phase particles observed in Section 3.1 act as effective pinning points for dislocations, contributing to strengthening through particle–dislocation interactions and increased dislocation storage during deformation [23]. The combined effect of these two mechanisms —work hardening and particle strengthening—accounts for the substantial enhancement in strength and hardness.

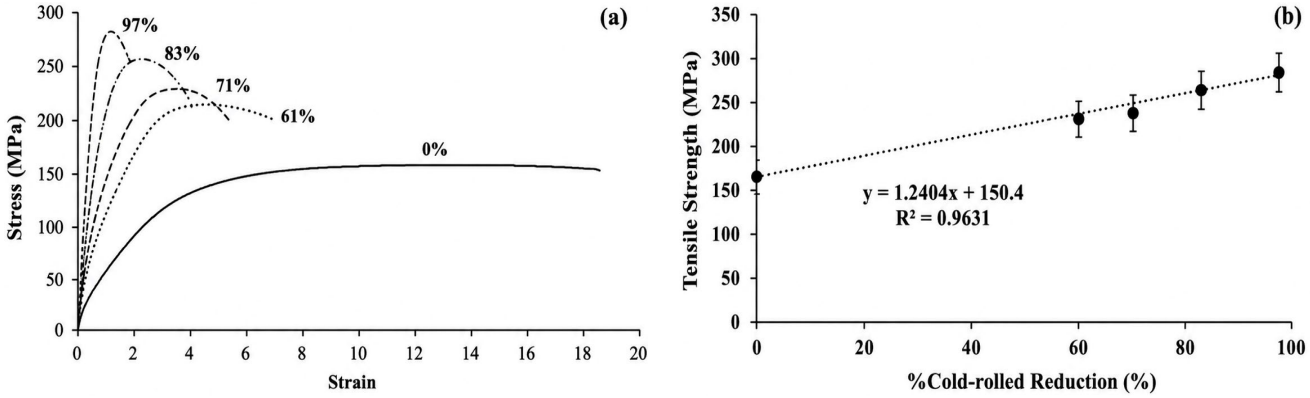


Figure 2. (a) Stress-strain curve (b) Tensile strength of the samples in different degree of cold-rolled reduction in the parallel to RD: 0%, 61%, 71%, 83%, and 97%.

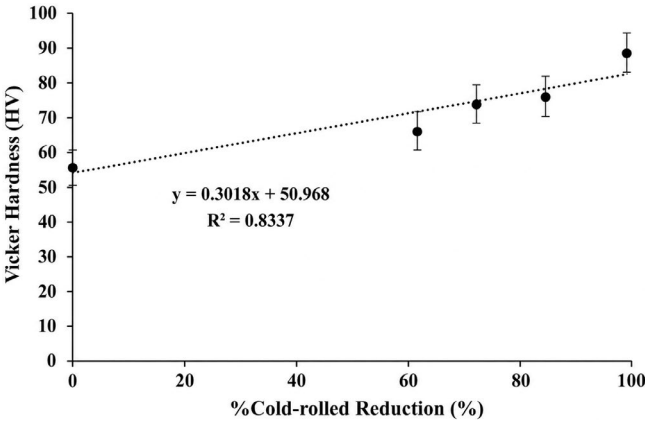


Figure 3. Evolution of Vickers microhardness at cold-rolling reductions of 0%, 61%, 71%, 83%, and 97%, measured on the RD–TD plane (normal parallel to ND).

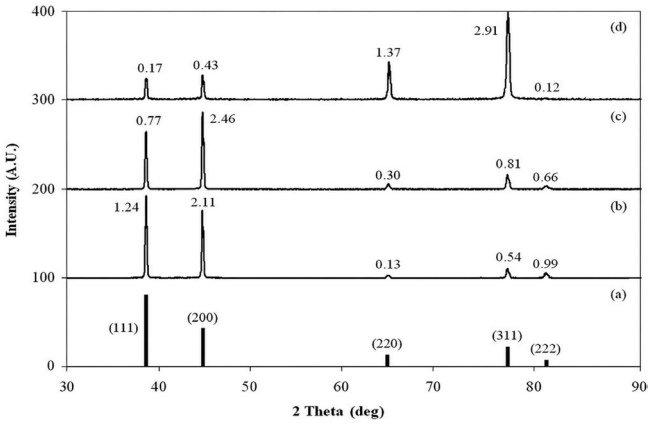


Figure 4. XRD patterns and pole densities of the samples in difference degree of cold-rolled reduction: (a) aluminum standard pattern, (b) 0%, (c) 61%, and (d) 97%.

Table 2. XRD patterns and pole densities of aluminum AA8006 with the increasing of cold-roll reduction.

Sample	2θ	I%	(hkl)	Pole density
0% cold-rolled reduction (As cast)	38.461	100.00	(111)	1.24
	44.703	79.90	(200)	2.11
	65.099	2.30	(220)	0.13
	78.201	10.40	(311)	0.54
	82.401	5.60	(222)	0.99
61% cold-rolled	38.459	66.50	(111)	0.77
	44.699	100.00	(200)	2.46
	65.100	5.80	(220)	0.30
	78.201	16.80	(311)	0.81
	82.419	4.00	(222)	0.66
71% cold-rolled reduction	38.439	72.40	(111)	0.86
	44.699	100.00	(200)	2.54
	65.059	5.40	(220)	0.29
	78.163	11.40	(311)	0.57
	82.362	4.30	(222)	0.73
83% cold-rolled reduction	38.403	48.00	(111)	0.35
	44.644	100.00	(200)	1.56
	65.059	38.70	(220)	1.29
	78.161	48.20	(311)	1.47
	82.366	3.20	(222)	0.33
97% cold-rolled reduction	38.460	24.40	(111)	0.17
	44.687	28.80	(200)	0.43
	65.100	43.30	(220)	1.37
	78.255	100.00	(311)	2.91
	82.392	1.20	(222)	0.12

3.3 Crystallographic texture development

3.3.1 Macrotexture evolution from XRD

The calculated TC values for key crystallographic planes, derived from XRD data, are summarized in Table 2 and graphically represented in Figure 4. In the as-cast 0% reduction condition, TC values for {111} and {200} planes are greater than 1 (1.24 and 2.11, respectively), indicating a preferential alignment of these planes parallel to the sample surface (ND). Conversely, {220} and {311} planes have TC values significantly below 1, indicating they are suppressed. With progressive cold rolling, a systematic and dramatic texture transition occurs. The preferential alignment of {111} and {200} plane normals with ND weakens sharply. For instance, TC{111} decreases from 1.24 at 0% reduction to 0.17 at 97% reduction. Concurrently, the initially suppressed {220} and {311} components intensify, with TC {311} rising from 0.54 to 2.91 at 97% reduction. This signifies a major reorientation of the crystal lattice. The pole figures provide a spatial visualization of this transition. Figure 5 shows the {111}, {200}, {220}, and {311} pole figures for the as-cast material, displaying relatively diffuse textures. Figure 6 tracks the evolution of the {111} pole figure with deformation. The as-cast sample shows a broad, near-maximum intensity at the center (ND). With 61% and 97% reduction, this maximum splits and shifts towards RD, forming distinct arcs. These changes are consistent with the development of rolling texture in FCC metals. The characteristic β-fiber connects the Brass ({110}<112>), S ({123}<634>), and Copper ({112}<111>) components in orientation space [11,13,24]. Here, the XRD pole figures provide the primary basis for interpreting bulk texture evolution, while TC values quantify changes in the preferred alignment of selected plane normals. These results are consistent with β-fiber development, but the pole figures and TC values presented here do not independently establish a continuous three-dimensional β-fiber or quantify the individual component fractions. Texture may influence the tensile response along RD; its contribution is considered alongside the work-hardening and particle–dislocation mechanisms discussed in Section 3.2 [24,25].

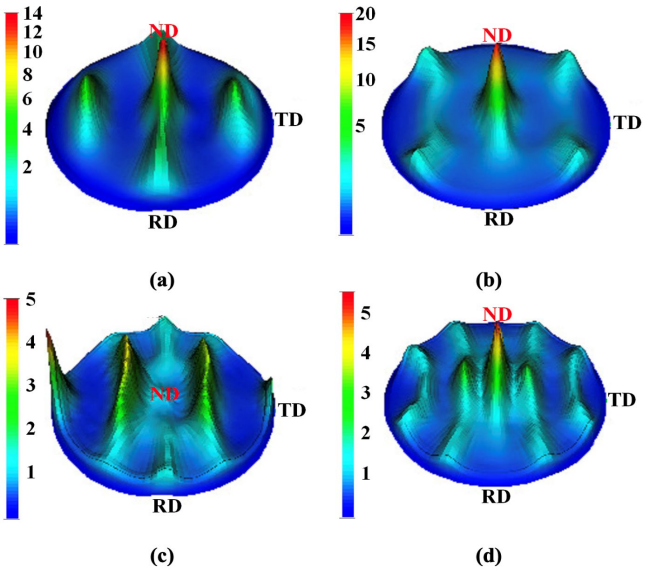


Figure 5. Pole figure of the sample as-cast 0% cold-rolled reduction in difference planes: (a){111}, (b){200}, (c){220}, and (d){311}.

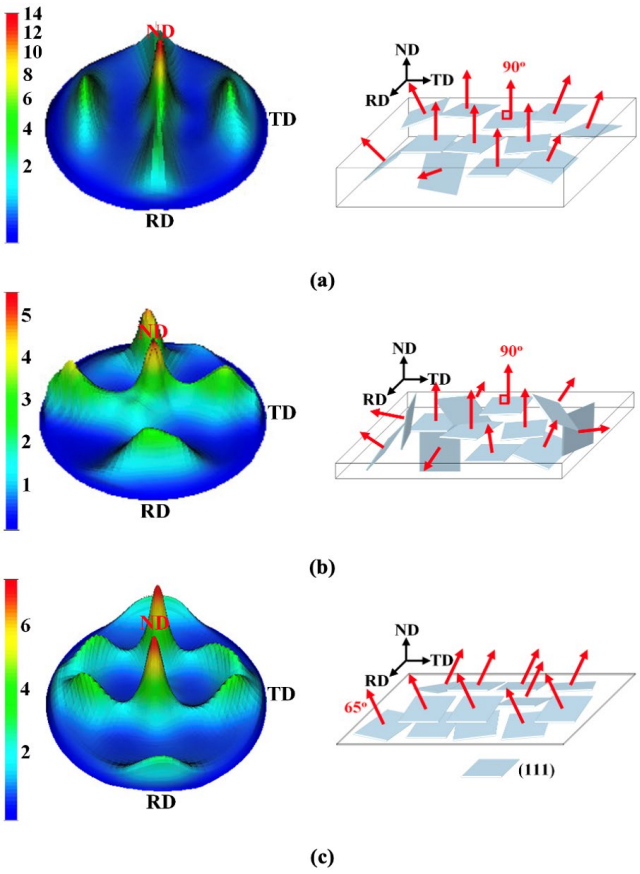


Figure 6. Pole figure and schematic illustration in plane {111} of the samples in different degree of cold-rolled reduction: (a) 0%, (b) 61%, and (c) 97%.

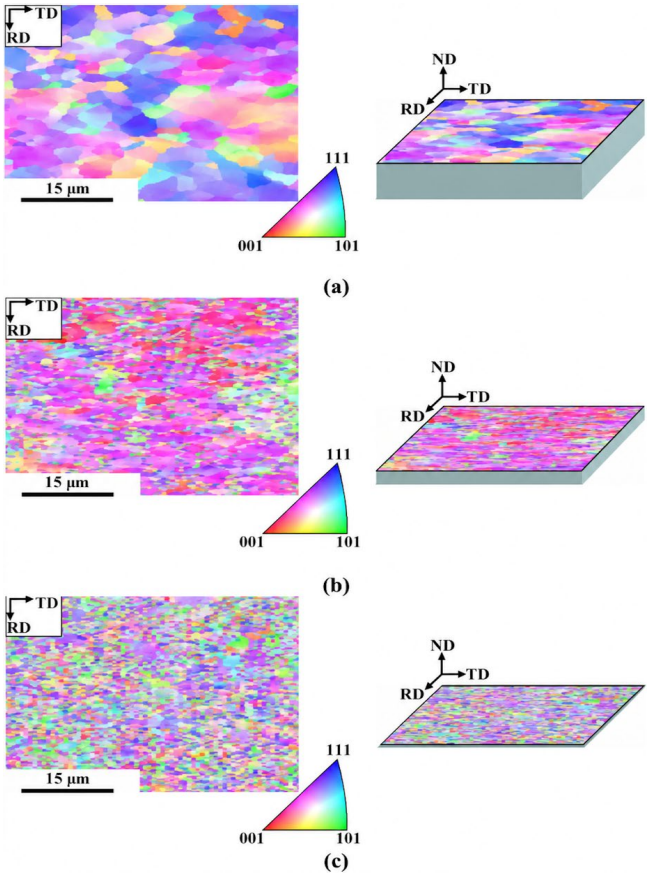


Figure 7. IPF maps colored with respect to ND and schematic illustration of the samples in different degree of cold-rolled reduction: (a) 0%, (b) 61%, and (c) 97%.

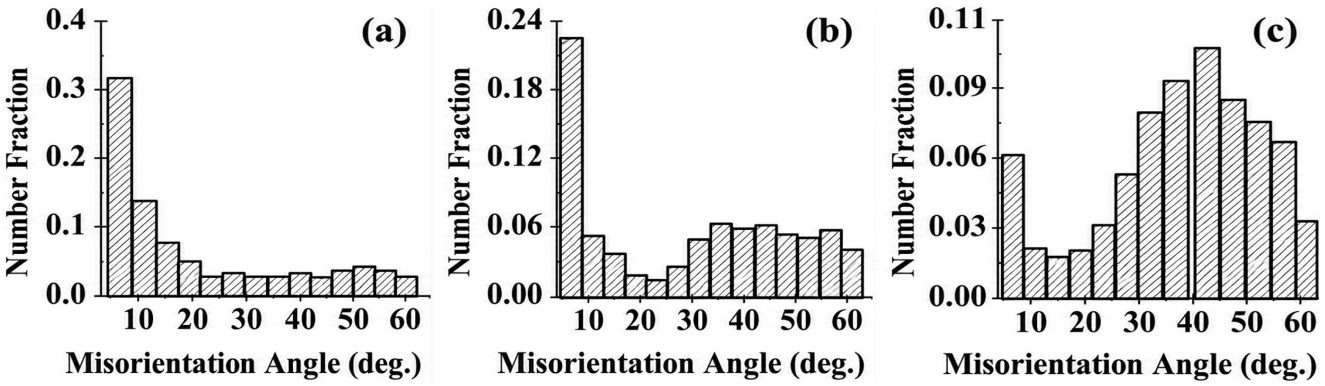


Figure 8. Misorientation angle of the samples in different degree of cold-rolled reduction: (a) 0%, (b) 61%, and (c) 97%.

3.3.2 Microtexture and substructure from EBSD

EBSD analysis provides complementary, local-scale insights into orientation and substructure evolution. The IPF maps in Figure 7 are colored according to the crystallographic direction parallel to ND and show grain morphology and local orientation variations in real space. They do not represent the full three-dimensional orientation distribution in Bunge Euler space (φ_1, Φ, φ_2). In this study, the quantitative assessment of preferred plane-normal alignments relies primarily on the XRD TC values, and the interpretation of bulk rolling-texture evolution relies on the XRD pole figures (Section 3.3.1). EBSD IPF maps are used to observe grain elongation and local orientation gradients, together with the boundary misorientation distributions in Figure 8. No EBSD-derived orientation distribution function (ODF) sections or β-fiber orientation-density profiles are presented; therefore, continuous β-fiber development and the relative densities of the Copper, S, and Brass components are not quantitatively verified by the EBSD maps [11]. The as-cast sample (0% reduction) shows relatively large grains with a variety of IPF colors, indicating a range of crystal directions aligned with ND. After 61% reduction, the grains are elongated into thin lamellae parallel to RD. Color variations within individual lamellae indicate local orientation gradients associated with grain subdivision. At 97% reduction, the microstructure consists of a dense array of fine, elongated features. Regions of similar color indicate similar crystal

directions parallel to ND. Such color groupings alone cannot distinguish complete texture components, such as Cube or Goss, because the in-plane crystallographic orientation is not uniquely specified by an ND IPF color [11].The misorientation angle distributions provide additional information about the deformation substructure (Figure 8). The as-cast sample shows a high frequency of high-angle boundaries (>15°) and a peak near 60°. With cold rolling, a pronounced peak develops at 45° to 50° for the 61% and 97% reduced samples. These changes indicate an evolving distribution of boundary misorientations during deformation. Misorientation angles alone do not uniquely identify twin boundaries or specific pairs of β-fiber components; establishing such relationships requires the corresponding rotation axes and full grain orientations [11,26]. The EBSD results therefore complement the XRD macrotexture analysis by documenting local morphology, orientation gradients, and boundary misorientation distributions.

4. Conclusions

Severe cold rolling effectively enhanced the strength and hardness of AA8006 aluminum alloy, with the highest reduction level (97%) producing the greatest mechanical improvement due to the accumulation of deformation-induced defects.

Progressive fragmentation and redistribution of Al–Fe–Mn–Si intermetallic particles modified the deformation behavior of the alloy and contributed to strengthening through particle–dislocation interactions.

Crystallographic characterization revealed substantial changes in grain orientation and deformation substructure with increasing rolling reduction, demonstrating the strong influence of plastic deformation on microstructural evolution.

The results establish a clear relationship between processing conditions, microstructural evolution, and mechanical performance, providing useful guidance for optimizing the cold-rolling process of AA8006 and related non-heat-treatable aluminum alloys.

The XRD results show changes in bulk preferred orientation that are consistent with rolling-texture development, while EBSD reveals local orientation variations and deformation substructure. The texture observations complement the strengthening mechanisms discussed for the tensile response along RD. ODF analysis is needed to quantify the continuous β-fiber and its components, and multi-directional mechanical testing is required to evaluate anisotropy.

Acknowledgements

The authors gratefully acknowledge the Research, Innovation Unit of Rail System and Testing (RU-RailS) and the Center of Excellence in Professional Skills and Technology (CoE), Faculty of Engineering, Rajamangala University of Technology Lanna, for providing laboratory facilities and technical support. The material supply from the Department of Metallurgical Engineering, Chulalongkorn University, is also sincerely appreciated.

References

[1] F. Czerwinski, "Aluminum alloys for electrical engineering: A review," *Journal of Materials Science*, vol. 59, no. 32. pp.14847–14892, 2024.

[2] J. Hirsch, and T. Al-Samman, "Superior light metals by texture engineering: Optimized aluminum and magnesium alloys for automotive applications," *Acta Materialia*, vol. 61, no. 3, pp. 818–843, 2013,

[3] T. Jin, H. Xiao, L. Ding, X. Zhao, X. Lei, B. Wan, Y. Weng, Z. Jia, and Q. Liu, "Microstructure and texture evolution in aluminum alloys," *Materials Characterization*, vol. 200, p. 112857, 2023.

[4] X. Gong, H. Li, S. B. Kang, J. H. Cho, and S. Li, "Texture and microstructure evolution during rolling of aluminum alloys," *Materials & Design*, vol. 31, pp. 1581–1587, 2010.

[5] Z. Li, J. Peng, J. Zhang, X. Chen, Q. Shan, S. Han, and F. Zhang, "Revealing the microstructure, texture evolution mechanism and mechanical properties of cryogenic rolled and microtherm aged AA6061," *Journal of Manufacturing Processes*, vol. 120, pp. 205–221, 2024.

[6] R. Kumar, A. Gupta, T. R. Dandekar, and R. K. Khatirkar, "Evolution of microstructure and texture during homogenization in a strip cast AA8011 aluminum alloy," *Intermetallics*, vol. 130, p. 107064, 2021.

[7] G. Gao, X. Li, B. Xiong, Z. Li, Y. Zhang, Y. Li, and L. Yan, "Effect of deformation on aluminum alloy microstructure," *Materials*, vol. 15, p. 5638, 2022.

[8] Z. Wu, H. Bei, F. Otto, G. M. Pharr, and E. P. George, "Microstructural evolution and strengthening mechanisms," *Intermetallics*, vol. 46, pp. 131–140, 2014.

[9] N. B. Dahotre, "Surface modification and material processing," *Materials Manufacturing Processes*, vol. 14, pp. 903–905, 1999.

[10] R. K. Ray, J. J. Jonas, and R. E. Hook, "Cold rolling and annealing textures in low carbon and extra low carbon steels," *International Materials Reviews*, vol. 39, pp. 129–172, 1994.

[11] O. Engler, S. Zaefferer, and V. Randle, "Introduction to texture analysis: Macrotexture, microtexture, and orientation mapping, 3rd ed. Boca Raton, FL, USA: CRC Press, 2024,

[12] A. B. Lopes, F. B. Barlat, J. Grácio, J. F. Duarte, and E. F. Rauch, "Effect of crystallographic texture on plastic anisotropy," *International Journal of Plasticity*, vol. 19, pp. 1–22, 2003.

[13] Z. Bojar, P. R. Jóźwik, K. Karczewski, and W. Polkowski, "Microstructure and texture evolution in metallic materials," *Archives of Civil and Mechanical Engineering*, vol. 14, pp. 550–559, 2014.

[14] S. Sadi, A. Hanna, T. Baudin, A. L. Helbert, F. Brisset, D. Bradai, and H. Azzeddine, "Evaluation of static recrystallization and grain growth kinetics of hot-rolled AZ31 alloy," *Journal of Metals, Materials and Minerals*, vol. 32, no. 1, pp. 12–26, 2022.

[15] W. Boonchouytan, J. Chatthong, and R. Burapa, "Analysis of the impact factors from the friction stir welding process for dissimilar butt joints between semi-solid cast aluminum 356 and AISI 1018 carbon steel," *Journal of Metals, Materials and Minerals*, vol. 31, no. 2, pp. 1–9, 2021.

[16] S. Hamza, Z. Boumerzoug, A. L. Helbert, F. Bresset, and T. Baudin, "Texture analysis of welded 304L pipeline steel," *Journal of Metals, Materials and Minerals*, vol. 29, no. 3, 2019.

[17] ASTM International. Standard Practice for Microetching Metals and Alloys. ASTM E407-07(2015)e1. West Conshohocken, PA: ASTM International, 2015.

[18] N. Jantaping, C. A. Schuh, and Y. Boonyongmaneerat, "Influences of crystallographic texture and nanostructural features on corrosion properties of electrogalvanized and chromate conversion coatings," *Surface and Coatings Technology*, vol. 329, pp. 120–130, 2017.

[19] N. Jantaping, C. Banjongprasert, T. Chairuangsri, U. Patakham, and Y. Boonyongmaneerat, "Challenges and strategies of surface modification of electrogalvanized coatings for electron microscopy analysis," *Micron*, vol. 86, pp. 48–53, 2016.

[20] P. Moldovan, G. Popescu, and F. Miculescu, "Microscopic study regarding the microstructure evolution of the 8006 alloy in the plastic deformation process," *Journal of Materials Processing Technology,* vol. 153–154, pp. 408–415, 2004.

[21] O. Matvienko, O. Daneyko, T. Kovalevskaya, A. Khrustalyov, I. Zhukov, and A. Vorozhtsov, "Microstructure evolution in metallic systems," *Metals*, vol. 11, p. 279, 2021.

[22] N. Hansen and D. Juul Jensen, "Development of microstructure in FCC metals during cold work," *Philosophical Transactions of the Royal Society A*, vol. 357, pp. 1447–1469, 1999.

[23] A. J. Ardell, "Precipitation hardening," *Metallurgical Transactions A*, vol. 16, pp. 2131–2165, 1985.

[24] O. Engler, and J. Hirsch, "Texture control by thermomechanical processing of AA6xxx Al-Mg-Si sheet alloys for automotive applications," *Materials Science and Engineering A*, vol. 336, pp. 249–262, 2002.

[25] H. Jazaeri, and F. J. Humphreys, "Recrystallization kinetics and texture evolution," *Acta Materialia*, vol. 52, pp. 3251–3262, 2004.

[26] Q. Liu, and N. Hansen, "Macroscopic and microscopic subdivision and local misorientation in cold-worked metals," *Proceedings of the Royal Society A*, vol. 454, pp. 2555–2592, 1998.